CITATION

MLA: Clarke, M., and Alonso. J. J., "Lithium–Ion Battery Modeling for Aerospace Applications" Journal of Aircraft, Vol. 58, No. 6 (2021), pp. 1323-1335

BibTex
```
@article{clarke2021lithium,
title={Lithium-ion battery modeling for aerospace applications},
author={Clarke, Matthew and Alonso, Juan J},
journal={Journal of Aircraft},
volume={58},
number={6},
pages={1323-1335},
year={2021},
publisher={American Institute of Aeronautics and Astronautics}
}
```

Lithium-Ion Battery Modeling for Aerospace Applications

Matthew Clarke* and Juan J. Alonso [†]

Department of Aeronautics and Astronautics, Stanford University, Stanford CA, 94305

In this paper we develop a semi-empirical model for predicting degradation in lithium-ion batteries and use it to assess the performance of an all-electric General Aviation aircraft over its operational lifetime. The model comprises three parts: a cycle discharge model, a heat-transfer model and a cell-aging model. The discharge model captures steady-state and transient behavior of the cell. The heat transfer model enables accurate prediction of the cell temperature within the modules of the battery pack. Lastly, the cell-aging model utilizes the electrical and thermal load profiles along with experimentally-obtained parameters to estimate battery degradation. A flight profile representative of a mission for this class of aircraft is then studied to assess the performance of the battery pack under realistic conditions. Preliminary results indicate that battery life of the aircraft operating a daily service of four regional flights can fall by as much as 25% after one calendar year. The sensitivities of discharge rate and cycle depth of discharge to factors such as flight trajectory and environmental conditions are subsequently examined. This detailed approach to battery modeling at the conceptual design stage is critical for appropriately sizing a battery system to meet the desired range and performance requirements over the entire duration of service.

Nomenclature

ρ	=	density $\left(\text{kg/m}^2\right)$
σ	=	thermal conductivity (S/m)
A_e	=	electrode area $\left(\text{m}^2\right)$
A_s	=	battery surface area $\left(\text{m}^2\right)$
c_p	=	specific heat capacity (J/kgK)
C_{Th}	=	Thevenin equivalent capacitance (F)

---

*Doctoral Candidate, Department of Aeronautics and Astronautics, AIAA Member Student Member.

[†]Professor, Department of Aeronautics and Astronautics, AIAA Associate Fellow.

D	=	diameter of battery cell (m)
DOD	=	depth of discharge
E_{Fade}	=	battery energy-capacity fade factor
F	=	Faraday constant, 96,485 (C/mol)
h	=	convective heat transfer coefficient $(\text{W/m}^2\text{K})$
H	=	height of battery cell (m)
i	=	current density (A/m^2)
I_L	=	load current (A)
n	=	charge number pertaining to the reaction
$MTOW$	=	maximum takeoff weight (lb)
Q	=	charge throughput (A-hr)
$\dot{q}$	=	heat generated/loss (W)
R_0	=	ohmic resistance (Ω)
R_{Growth}	=	battery internal resistance growth factor
R_{Th}	=	polarization resistance (Ω)
SOC	=	state of charge
SOH	=	state of health
T_{amb}	=	ambient temperature (K)
T_{bat}	=	battery temperature (K)
V_{OC}	=	open-circuit voltage (V)
V_{Th}	=	Thevenin equivalent voltage (V)
V_{UL}	=	under-load voltage (V)

I. Introduction

Aᴄᴄᴏʀᴅɪɴɢ to the Environmental Protection Agency [1], light-weight vehicles such as personal cars and ride-shares stand as the leading contributors to greenhouse gas emissions within the U.S. However, in examining the projected growth in the number of air travelers over the next two decades [2], the anticipated contribution of emissions from the aviation industry cannot be overlooked. In response, governments and private entities are looking for ways to minimize their carbon footprint using biofuels and electrification. Notably, there has been an emphasis on curtailing emissions through the deployment of lithium-ion battery-powered aircraft, in part made possible by advancements in material science that have led to the creation of high-energy-density batteries [3–8]. The potential cost savings summarized in Table 1 present the compelling case to transition away from less efficient internal combustion engine (ICE) technology. Here, we see that the price of refining raw materials and supplying hydrocarbon fuel for the use in ICE aircraft is roughly six times higher than the price of producing and supplying an equivalent unit of electrical energy for

use in electric aircraft. Adding in the fuel burn of ICEs during flight operations, we begin to see stark differences in the quantities of greenhouse gases emitted into the atmosphere.

Table 1   Comparison of ICE to DEP Aircraft Architectures [9].

	Internal Combustion Engine (ICE)	Distributed Electric Propulsion (DEP)
Average cost of fuel per hour	$200	$35
Average operating costs per hour	$440	$275
% Operating cost per hour for energy	45%	9%
Greenhouse gases emission	90 kg (CO_2)/hour	10 - 24 kg (CO_2)/hour

However, despite the concerted effort to integrate transformative battery technologies into vehicle propulsion architectures, several lingering challenges have led to creeping progress towards realizing all-electric aircraft. Many of these challenges stem from oversimplifications made during the conceptual design stage of new aircraft. For instance, the use of models incapable of capturing electrical load modulation experienced in flight as well as pack-level assumptions made when estimating cell temperature can result in disagreement between aircraft designers and battery experts on the performance ceilings of electrochemical cells. This disconnect will become even more apparent in urban air mobility (UAM) operations which intend to deploy electric vertical takeoff and landing (eVTOL) aircraft that consume large amounts of energy during transitioning approach and departure procedures [10]. Furthermore, with go-around maneuvers, weather-related alternative landings and congestion at vertiports, realistic UAM operations can lead to significant departures from the standard eVTOL power profiles.

There are also many challenges associated with the electrochemical cell itself. These include the creation of a safe, non-flammable electrolyte with a large operating window and the formation of an amorphous solid/electrolyte-interface (SEI) layer which develops as a result of repeated cycling [11]. During each cycle when the cell is fully charged, the electrolyte and electrode become more reactive and can react with one another, forming this passivating SEI layer containing lithium. Although this byproduct coats and protects the electrodes preventing further corrosive reactions, it is irreversible. The consumption of lithium ions to form this SEI layer reduces the concentration of ions to facilitate energy storage, resulting in a reduction in the overall energy-capacity [12, 13]. Failure to capture this diminishing behavior can therefore bring about an over-prediction of system-level performance which can lead to the inability of an electric vehicle (EV) to meet its intended range. As a result, battery-life studies should be considered an important practice for evaluating long-term flight operations and estimating market potential.

To address the aforementioned shortcomings, a three-stage semi-empirical model is proposed. This first stage is a electrical discharge model capable of capturing the steady-state and transient

responses of the battery during charging and discharging. The second stage is a thermal model that applies principles of forced-convection to quantify the thermal load on individual cells. The last stage estimates the simultaneous decay of the cell's energy-capacity and increase in internal impedance. This detailed approach to capturing transport phenomena within the cell during continuous operation falls between simple first-order approximations and more computationally-intensive methods such as finite element analysis, thus earning the classification of medium-fidelity. These methods provide acceptable accuracy compared to higher-fidelity methods at a fraction of the computational cost, making them attractive for iterative design approaches. When collectively used to model the energy network of an electric aircraft, they allow the designer to capture important electrophysical and electrothermal behavior that may go unseen at the system-level. This comprehensive model is then used to assess the performance of a battery pack of an all-electric General Aviation (GA) aircraft given its flight profile and operating atmospheric conditions. Implementation of this model into SUAVE, an open-source conceptual aircraft design tool developed and maintained by the Aerospace Design Lab at Stanford University is also documented. The sensitivities of the discharge rate, state of charge (SOC) and state of health (SOH) to environmental conditions, aircraft range and rates of climb are subsequently quantified and discussed.

II. Categorizing Lithium-ion Batteries

Compared to other battery technologies such as molten salts and lithium-air, reliability in performance coupled with high energy and power densities have led to rechargeable lithium-ion batteries being the preferred energy source for EVs [14, 15]. Due to high demand, mostly driven by consumer electronics and the automotive industry, low manufacturing cost has also made it easier to develop and test battery packs based on such technology. The primary components of this electrochemical cell are; (1) a cathode, (2) an anode, separated by (3) an electrolyte that is connected to (4) current collectors as shown in Figure 1. During electrical discharge to an externally connected circuit, there is simultaneous diffusion of lithium ions occurring within the cell from the anode to the cathode through the electrolyte.

For EV applications, lithium-ion cells are commercially produced as either the prismatic pouch cells, constructed as successive layers of electrode, electrolyte and current collector, or as jelly-rolled cylindrical cells. Both have their advantages and disadvantages. For example, the pouch cell has a large surface area suitable for cooling, but requires a heavy protective case which adds a significant amount of weight to the overall battery pack. On the other hand, the cylindrical cell offers durability, but at the expense of low packaging density. Further classification of lithium-ion batteries is done by the chemical compound used at the positive electrode – with long cycle-life, graphite remains as the best negative electrode today. A comparison of common cathode compounds by [16] is provided
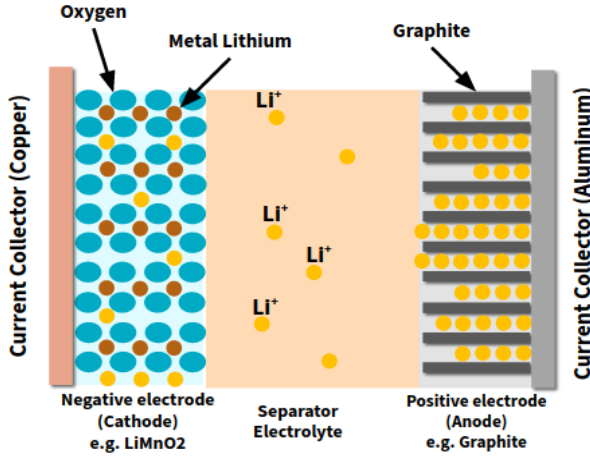
5

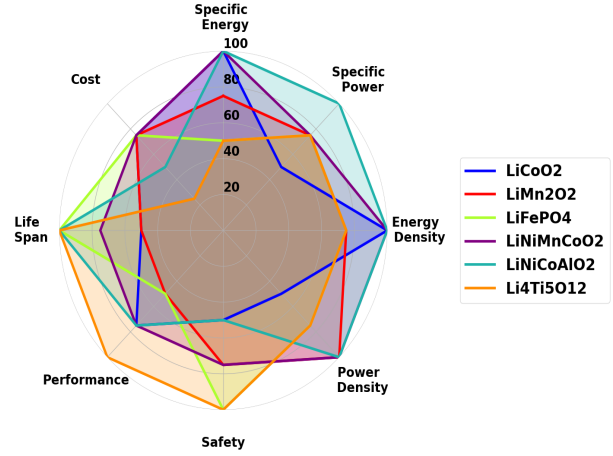**Fig. 1   Structure of a lithium-ion battery cell.**

Fig. 2   Comparison of lithium-ion battery chemistries.

in Figure 2. With high scores in safety and lifespan, we can infer why lithium-iron-phosphate (stoichiometry: $LiFePO_4$, abbreviated LFP) is used in many ground transportation EV applications such as buses where weight is not a major design concern. However, in aerospace applications where weight is a limiting factor, cathodic chemistries such as lithium-nickel-manganese-cobalt-oxide (stoichiometry: $LiNiMnCoO_2$, abbreviated NMC) and lithium-nickel-cobalt-aluminum oxide (stoichiometry: $LiNiCoAlO_2$, abbreviated NCA) are preferred. The NMC cell has a similar energy and power density to the NCA cell, but outperforms the NCA cell in the metrics of safety and cost of sourcing raw materials for cell manufacture. In this study, the cylindrical NMC cell developed by Panasonic is used in the computational model of the lithium-ion cell.

III. Current State of Lithium-ion Battery Modeling

In this study, we define an electrochemical cell as the smallest independent source of stored-energy and a battery module as a collection of these cells electrically connected in some regular arrangement. Likewise, a battery pack is made up of modules to form the unified energy source of an EV. Furthermore, SOC is defined as the energy remaining within an individual cell or entire battery pack as a percentage of its fully-charged state, whereas SOH refers to the figure of merit of the condition of the battery relative to its ideal (initial) condition. The battery management system (BMS) in EVs is responsible for estimating both the SOC and SOH of individual cells within the pack. The most frequently used methods for estimating SOC are documented in Table 2.

Moreover, all batteries have an ideal temperature range for optimal operation. Below this range, the battery's energy-capacity decreases and above this range the potential of a safety hazard significantly heightens. The speed at which fires can erupt and the catastrophic nature of these explosions make thermal runaway an important issue in lithium-ion battery use. Accordingly, it

Table 2   Methods of estimating SOC.

Method	Pros	Cons
Curve Fitting [17]	Simple with few function parameters; desirable for data-driven modeling	Low accuracy at high and low SOC; does not consider physical mechanics of cell discharge
Equivalent Circuit Modeling [18–20]	Simple with acceptable accuracy; desirable for simulation and BMS use	Chemistry and cell structure specific
Coulomb Counting [21–23]	High accuracy	Reliance on high-precision sensors; can accumulate large errors due to uncertainties or disturbances
Kalman Filter [24–26]	High accuracy; able to predict thermal gradients within cell	Computationally-intensive

is crucial to monitor and control the temperature of a battery by means of a thermal management system that ensures operation within safe margins to prolong cycle-life. To design a robust BMS, the cell behavior must therefore not only be characterized at optimal conditions but in off-design conditions that reflect the temperature fluctuations in different geographic locations around the world. This includes cities that have cold climates due to latitude or altitude such as Moscow and Denver respectively, as well as cities where temperatures can soar over 40 °C (104 °F) such as Sydney.

The use of computational modeling to predict heat generation and assess cooling strategies to remove battery-generated heat has proven to be an efficient and cost-effective method of extending shelf life [27]. For example, [28] sought to prolong battery life by minimizing thermal runaway through natural and forced cooling strategies. This work was extended by [29] in their assessment of the impact of cubic, hexagonal and circular cell arrangements on the maximum pack temperature. However, in the two previously-mentioned studies, the discharged current was held constant. [30] was one of the first studies to use a power profile of an electric vehicle, thus generating a more realistic thermal profile of the battery pack. In this current study, SUAVE is used in a similar manner to generate the realistic power profiles that the battery of an electric GA aircraft would experience during flight.

Finally with respect to cell aging, the two established approaches to forecasting SOH are the physics-based electrochemical model and the semi-empirical degradation model. The former utilizes physical principles to describe mass transfer, charge transfer and by-product deposition within the battery while the latter uses observed parameters to derive relations for characterizing aging. The benefits and disadvantages of each degradation model are summarized in Table 3.

Since we will be examining one type of lithium-ion cell under various operating conditions, the

Table 3   Methods of forecasting SOH.

Method	Pros	Cons
Physics-based Electrochemical Model [31, 32]	High accuracy; desirable for data-driven modeling	Computationally-intensive
Semi-empirical Degradation Model [33, 34]	Simple with acceptable accuracy; suited for real-time estimation, simulation and BMS control-law development	Chemistry and cell structure specific

semi-empirical degradation model was the preferred approach. The degradation model detailed below was inspired by [35] and [36] and possesses several attractive characteristics including the ability to capture the influence of temperature and voltage on calendar aging, as well as the effect of depth of discharge (DOD) and SOC on cycle aging.

IV. Electric Propulsion Network Battery Modeling

A. Electrical Discharge/Charge Model

The equivalent circuit model presented below is based on the Thevenin circuit and is capable of characterizing key electric properties such as the transient response during the battery charge-discharge cycle. This is critical for predicting battery performance under the high-frequency load modulation needed to stabilize the aircraft during flight. As shown in Figure 3a, the model comprises four components: the open-circuit voltage (V_{OC}), the ohmic resistance (R_0), the polarization resistance (R_{Th}) and the polarization capacitance (C_{Th}) which captures the transient response. The electrical properties of the NMC cell used in this study are provided in Table 4. [37] and [23] were used to model the electrical characteristics of this battery chemistry during discharge. More specifically, experimental data from [37] was used to generate a surrogate model for cell voltage as a function of temperature, current and SOC, while [23] provided models for the other state variables (R_0, R_{Th} and C_{Th}) essential for characterizing internal resistance growth during aging and polarization. The expressions for these state variables, provided in Equations (1a) to (1d), were developed by [23] using a Recursive Least Squares algorithm to fit experimental data obtained from pulse polarization tests.

Table 4   Properties of the Panasonic NCR18650G cell [37].

Parameter	Value
Nominal Voltage (V)	3.6
Nominal Capacity (mAh)	3550
Standard Charge (CC-CV)	1.305A - 4.2V
Diameter (mm)	18.5
Height (mm)	65.3
Weight (g)	48.0
Specific Heat Capacity (J/kgK)	1007

(a) Thevenin Equivalent Circuit.

(b) Schematic of cylindrical lithium-ion cell by [38].
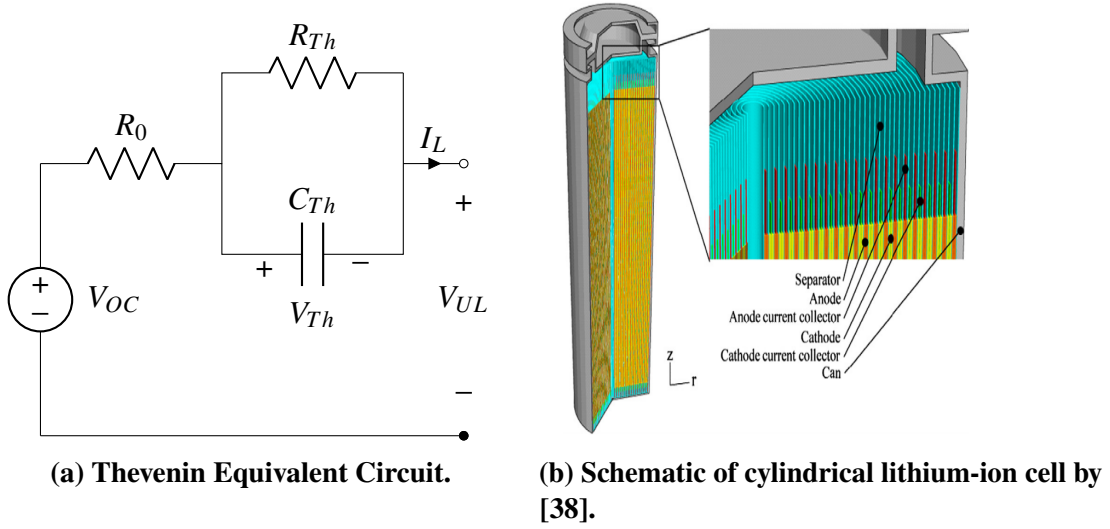
Fig. 3   Schematic of NMC cell

$$R_0 = 0.01483 SOC^2 - 0.02518 SOC + 0.1036 \tag{1a}$$

$$R_{th} = -1.212 e^{-0.03383 SOC} + 1.258 \tag{1b}$$

$$\tau_{th} = 2.151 e^{2.132 SOC} + 27.2 \tag{1c}$$

$$C_{th} = \frac{\tau_{th}}{R_{th}} \tag{1d}$$

Using the above expressions, the voltage across the parallel resistor-capacitor combination as well as the terminal voltage (V_{UL}) to the propulsion system and powered electronics can be computed as follows:

$$\frac{dV_{Th}}{dt} = \frac{I_L}{C_{Th}} - \frac{V_{Th}}{R_{Th}C_{Th}} \tag{2}$$

$$V_{UL} = V_{OC} - V_{Th} - I_L R_0 \tag{3}$$

B. Thermal Model

The thermal model presented below balances heat generation with convective heat dissipation into the surroundings. Within each cell, the temperature and heat-generation rate is determined through the conservation of energy and Gibbs function using a relation first proposed by [39] and detailed in Equations (4a) to (4c). The cell's temperature changes are captured through numerical expressions for the electrochemical reactions, phase changes, mixing effects and Joule heating. In this current study, four assumptions governing this heat generation were made. These were (1) the homogeneity of the cell's internal structure; (2) the temperature independent thermophysical properties; (3) the uniform distribution of the internal heat source in all directions; and (4) the absence of thermal radiation and convective heat transfer within the battery cell. The first assumption was deemed acceptable based on work by [40–42] which demonstrated that a detailed cell structure had little effect on the thermal behavior of the battery. As a result, a single value was used to represent the specific heat capacity of the cell. Regarding the second assumption, studies in [43] suggest that properties such as freezing point, boiling point, viscosity and conductivity of the electrolyte and electrodes do not change significantly between 0°C and 50°C, allowing us to assume temperature independence. The third assumption was acceptable based on work by [44] which demonstrated that for small cylindrical lithium-ion cells, electrochemical properties inside the battery tend to be homogeneous and isotropic. The last assumption can be made given the limited mobility of the liquid electrolyte in a lithium-ion battery as pointed out by [45].

$$\dot{q}_{heat} = \dot{q}_{Joule} + \dot{q}_{entropy} \tag{4a}$$

$$\dot{q}_{Joule} = A_e i(V_{OC} - V_{UL}) = \frac{i^2}{\sigma} \tag{4b}$$

$$\dot{q}_{entropy} = -I\left(T\frac{\delta V_{OC}}{\delta T}\right) = -T\Delta S\frac{i}{nF} \tag{4c}$$

The first term on the right-hand side of Equation 4a accounts for the ohmic losses inside the battery cell, the charge transfer overpotential at the interface and the mass transfer limitations. The second term is the entropy heat generation term, often referred to as the reversible heat term. Entropic heat is generated when the lithium content of the electrode changes, causing the entropy of the electrode materials to change. The electrode area is used to compute i, the current density. The entropy change for NMC, ΔS, is given as a function of SOC as obtained from [38]. This relationship is a sixth-order polynomial fit to experimental data obtained from [46].

$$\begin{aligned}\Delta S_{LiNi_xCo_yMn_zO_2} = &-496.66(SOC)^6 + 1729.4(SOC)^5 - 2278(SOC)^4 + 1382.2(SOC)^3 \\ &-380.47(SOC)^2 + 46.508(SOC) - 10.692\end{aligned} \tag{5}$$

The entire battery pack for the electric GA aircraft consisted of 6720 cells in an electrical arrangement inspired by the NASA X-57 Maxwell [47] and is provided in Table 5 below.

Table 5   Electrical connectivity within the battery pack.

Configuration	Series x Parallel	Units
Sub-module	1s x 24p	No. of cells
Module	20s x 1p	No. of sub-modules
Pack	7s x 2p	No. of modules

(a) Representative battery module with N_L **= 30,** N_T **= 16.**

(b) Staggered cell arrangement.
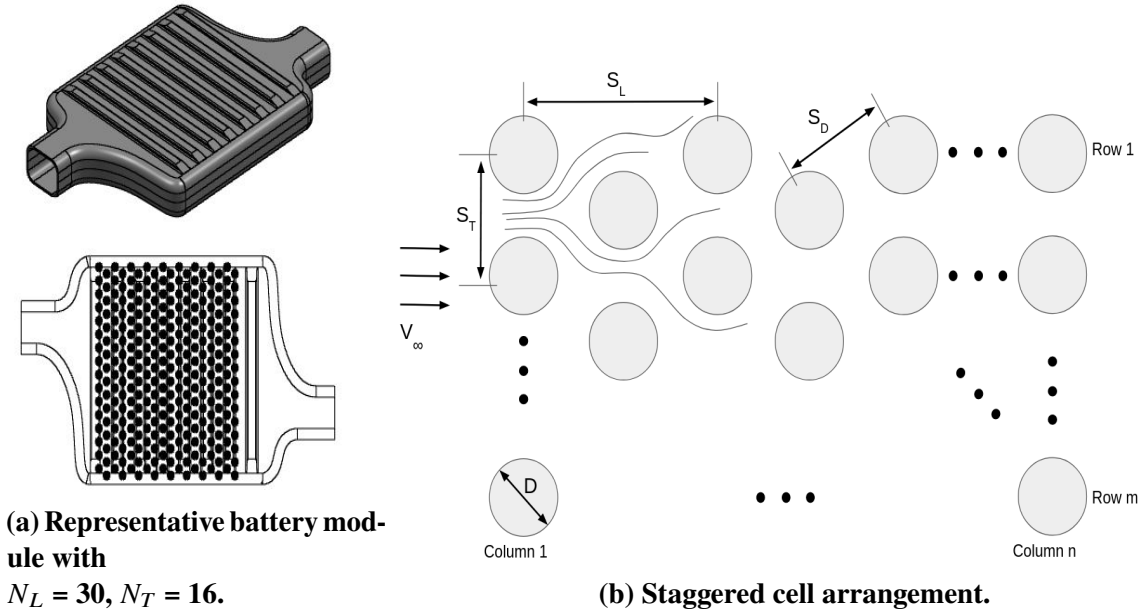
Fig. 4   Battery module design.

The thermal model examined behavior at the module-level. Atmospheric air was considered as the coolant within each battery module. Inside the modules, flow conditions are dominated by boundary-layer separation effects and turbulent wake interactions. Each module was modeled as a tube bank in a cross flow. Empirical formulations outlined in [48] were therefore used to estimate the heat removed from the system. Prior studies by [47] implemented a lumped model that oversimplified the configuration of the entire system, i.e. the geometry of the cell and the specific layout within the module was omitted. The use of such models that oversimplify the heat transfer between the coolant and battery cells prohibit any accurate analysis of thermal distribution within the pack, making any attempt to optimize performance futile. Additional assumptions regarding the layout of the battery module shown in Figure 4a were based on packs produced by Toyota [49]. Here, the simplest reduced-order model is employed where the battery cells can be considered to have the same temperature. The layout is characterized by the cell diameter, D, transverse pitch, S_T and

11

longitudinal pitch, S_L. Cell rows were staggered in the direction of the flow velocity, V_∞ as shown in Figure 4b. The values for these parameters used in this study are summarized in Table 6. These assumptions are appropriate for aircraft conceptual design as it provides sufficient information for a detailed analysis without introducing additional uncertainty.

The average heat transfer coefficient for the entire module can be determined using the relationship between Nu, which provides a measure of the convective heat transfer occurring at the surface of the cell, and Re, which represents the ratio of the inertia to viscous forces. This relationship is given below:

$$Nu = \frac{\tilde{h}D}{k_f} \tag{6}$$

Here, k_f is the thermal conductivity of the cooling fluid. Nu can be estimated through correlations by [50] based on Re characterizing the maximum flow in the tube bank, $Re_{D,max}$. The constants used in Equation 7 below can be found in [48] and are provided for different flow velocities and tube arrangements.

$$Nu = C Re_{D,max}^m Pr^{0.36} \left(\frac{Pr}{Pr_w} \right)^{0.25} \tag{7}$$

$$\text{where } \begin{cases} C = 0.35 \left(\frac{S_T}{S_L} \right)^{0.2} \text{ and } m = 0.6, & \text{if } Re_{D,max} > 1\text{x}10^3 \\ C = 0.51 \text{ and } m = 0.5, & \text{otherwise} \end{cases}$$

Pr and Pr_w are the Prandtl numbers of the fluid at the inlet and near the surface of the battery cells respectively. $Re_{D,max}$ are determined using S_T and S_L as follows:

$$Re_{D,max} = \frac{V_{max}D}{\nu} \tag{8}$$

$$\text{where } V_{max} = \begin{cases} V_\infty \frac{S_T}{2(S_D - D)}, & \text{if } 2(S_D - D) < (S_T - D) \\ V_\infty \frac{S_T}{(S_T - D)}, & \text{otherwise} \end{cases}$$

Here, the diagonal distance S_D can be determined as follows:

$$S_D = \sqrt{S_T^2 + S_L^2} \tag{9}$$

This model can be easily modified for in-lined tube bundles and different numbers of tubes (cells) parallel or perpendicular to the cooling flow. The temperature difference between the cell surface and the outlet temperature can then be determined using Equation 10, which, in turn, is used

Table 6   Geometry and coolant (air) flow conditions of the battery module.

Parameter	Value
V_∞ (m/s)	0.1
S_T (mm)	20
S_L (mm)	20
N_T	16
N_L	30

to determine the log mean temperature difference, ΔT_{LM}.

$$\frac{T_w - T_o}{T_w - T_i} = \frac{exp(-\pi D N_{tot} h)}{(\rho_\infty V_\infty N_T S_T c_{p_\infty})} \tag{10}$$

$$\Delta T_{LM} = \frac{(T_w - T_i) - (T_w - T_o)}{log\left(\frac{T_w - T_i}{T_w - T_o}\right)} \tag{11}$$

where N_{tot} is the total number of cells in the module and is given by $N_{tot} = N_T \times N_L = 16 \times 30 = 480$ cells in this case. The convective heat transfer from the battery can then be computed:

$$\dot{q}_{convec} = N_{tot} \tilde{h} A_s \Delta T_{LM} \tag{12}$$

The net heat load $\dot{q}_{net}$ and the cell temperature rise $\frac{dT}{dt}$ can be quantified using the following equations:

$$\dot{q}_{net} = \dot{q}_{heat} - \dot{q}_{convec} \tag{13a}$$

$$\frac{dT}{dt} = \frac{\dot{q}_{net}}{m C_p} \tag{13b}$$

C. Aging Model

The aging model presented below was developed by [36] and comprises two relations for the energy-capacity fade and internal resistance growth within the cell. This model fits a physics-based model to experimental data. It consists of an impedance-based electric-thermal model coupled with accepted metrics for predicting cell degradation. The electrical current profile, ambient air temperature and the depth of discharge are used to determine stress factors caused by volumetric changes during intercalation and deintercalation of lithium in the cathode and anode. This model

characterizing cell aging with time and repeated cycling is outlined below:

$$\alpha_{\text{cap}} = (7.543V - 23.75)10^6 e^{-\frac{6976}{T}} \tag{14a}$$

$$\alpha_{\text{res}} = (5.270V - 16.32)10^5 e^{-\frac{5986}{T}} \tag{14b}$$

$$\beta_{\text{cap}} = 7.348 10^{-3}(\text{Ø}V - 3.667)^2 + 7.600 10^{-4} + 4.081 10^{-3}\Delta\text{DOD} \tag{14c}$$

$$\beta_{\text{res}} = 2.153 10^{-4}(\text{Ø}V - 3.725)^2 - 1.521 10^{-5} + 2.798 10^{-4}\Delta\text{DOD} \tag{14d}$$

α_{cap} and α_{res} are calendar aging coefficients while β_{cap} and β_{res} below are cycle aging coefficients given as percentages. ØV is the quadratic-average voltage. The significance of this model is that it accounts for both the region of discharge (high and low voltages) as well as the cycle depth, making it suitable for quantifying the effect of EV power profiles. The superposition of calendar and cycle aging coefficients provides the total aging function for the battery energy-capacity fade and the internal resistance growth denoted E_{Fade} and R_{Growth} respectively. These parameters are given as normalizations to the initial state of the battery. Here, t is the aging time in days and Q is the charge throughput in Amp-Hours. Q can be interpreted as how much charge has passed through a battery cell in its lifetime.

$$E_{Fade} = 1 - \alpha_{\text{cap}}t^{0.75} - \beta_{\text{cap}}\sqrt{Q} \tag{15a}$$

$$R_{Growth} = 1 + \alpha_{\text{res}} t^{0.75} + \beta_{\text{res}} Q \tag{15b}$$

V. Model Validation

The approach taken to validate the computational methods used in this study was through the decomposition of the analyses by which the subcomponents of the vehicle are modeled. SUAVE is used for the aircraft-specific elements of this study. Validation studies in [51] highlight the accuracy of this tool for predicting both aerodynamic and propulsive performance of conventional and non-conventional aircraft in addition to estimating vehicle weight. Additionally, a comparative study by [52] using NASA's NDARC tool demonstrates SUAVE's ability to model propeller and rotor-driven propulsion networks with a battery system.

SUAVE implements a pseudospectral collocation method based upon the formation of generic differentiation (D) and integration (I) matrices for the integration of the trajectory of the aircraft across its mission. A full mission or flight profile is constructed by joining individual types of flight segments made up of control points in space and time. Pseudospec-

I. Simulation Set-up

1. Aircraft Parametrization: Define vehicle geometry, propulsion and energy networks.

2. Mission Parametrization: Assign atmospheric conditions and define flight profile.

3. Disciplinary Routines: Set-up aerodynamic, stability, structural and propulsion analysis methods.

II. Mission Solver

1. Non-linear Solver: Optimization of vehicle body angle, throttle and other propulsion network parameters at control points.

III. Post Processing

tral collocation is well-suited to general boundary-value problems and flexible enough to remain robust with any well-posed set of governing equations and boundary (or initial) conditions. A flowchart summarizing a typical simulation in SUAVE from geometry parametrization to post processing is given in Figure 5.

An all-electric GA aircraft with a conventional takeoff and landing approach is selected to assess the impact of medium-fidelity modeling of the battery pack. The geometry and specifications of this aircraft were inspired by the second modification of the NASA X-57 Maxwell – the wing-mounted twin-propeller variant. This aircraft is the agency's first all-electric experimental aircraft built to spearhead electric-propulsion-focused designs and airworthiness processes with regulators. The plane is constructed by modifying a baseline Italian Tecnam P2006T and consists of an electric powertrain powered by lithium-ion batteries. Shown in Figures 6 and 7 is a rendering of the Maxwell and a simplified model for analysis in SUAVE respectively. The lifting surfaces shown in Figure 7, each comprising 5 chordwise panels and 25 spanwise panels, are used in the Vortex Lattice Method (VLM) aerodynamic routine. To accelerate the computation time of solving the system of governing equations, surrogates of lift, drag and moment coefficient as a function of angle of attack and Mach number are first created during the initialization phase of the analysis routine. These response surfaces are then sampled by the mission solver at the control points. Aerodynamic validation of the aircraft used in this study is provided in Figure 8. The plots in 8a and 8b of lift curve slope and linearized drag polar respectfully illustrate close agreement with wind-tunnel tests performed by [53] of a 1:6.5 model of the Tecnam P2006T. At high angles of attack, we expect deviations from the experimental data as the VLM incorrectly assumes the flow remains attached over the surface of the wing. Corrections to the lift coefficient at high angles of attack as well as details concerning the calculation of parasitic and compressible drag components are outlined in [51].

In a similar vein, validation of the proposed medium-fidelity battery model was done through examination of its defining characteristics, notably the thermal loads arising the electrical discharge and cell aging. The inability to experimentally cycle an entire custom-made battery module over an extended period limited the scope of validation to the individual cells that constitute the pack. Consequently, one possible source of error in this work is the variance of the heat removed from the module. This will be tackled in future work through large-scale experimentation. Observed in Figure 9a is a comparison of the predicted thermal response of the NMC cell with experimental tests conducted by [38] when subjected to two different discharge rates. Similarly, the aging model was validated using experiments by [35] on a cell cycled at 35° C and 1C. Figure 9b depicts the
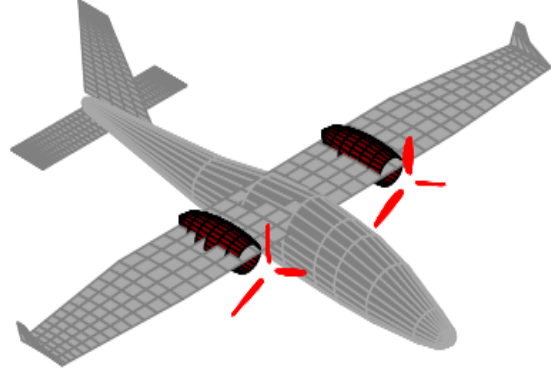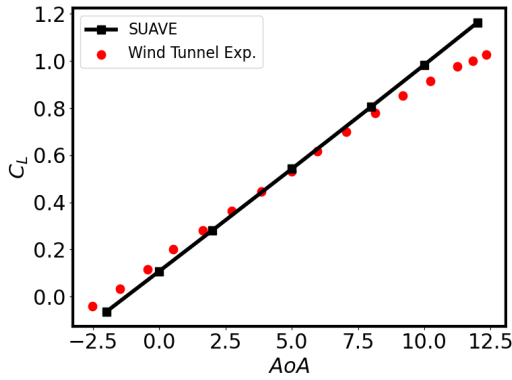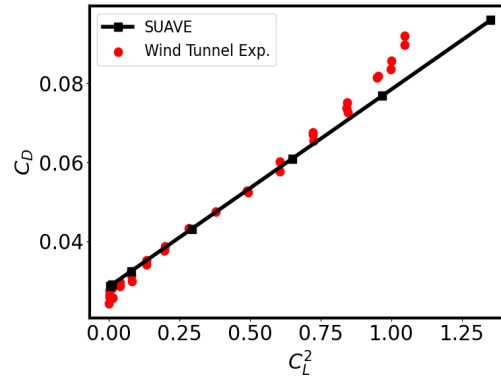
15

Fig. 6   NASA X57 Maxwell.

Fig. 7   SUAVE GA Aircraft Model.

(a) Aircraft lift curve.

(b) Aircraft linearized drag polar.

Fig. 8   Validation of twin-engine configuration aircraft.

depletion of energy-capacity as well as increase in internal resistance at various cycle depths. For example, a cycle depth of 75-25% implies that the cell was cycled from SOC of 0.75 to 0.25.

VI. Flight Profile Simulation

The medium-fidelity model outlined in Section IV form key portions of the propulsion network analysis routine used in the flight simulation. A summary of other high-level attributes of the aircraft is provided in Table 7. The mission profile is defined by the segments listed in Table 8 and a supplementary diagram is provided in Figure 10. The altitude and airspeed of the aircraft are displayed in Figures 11a and 11b respectively. The battery was initially sized to a range of 90 miles, representative of a nominal flight from San Francisco to Sacramento with a 10% reserve. As suggested by [52], a tech factor of 1.42, or 42% pack overhead mass fraction is used to account for the mass of the BMS, wiring and protective module housing. This resulted in a total battery pack mass of 458 kg. Based on the configuration of the sub-module, module and pack outlined in Table

(a) Cell temperature profile at constant C-rate and natural convection, $h = 7.17 W/m^2 K.$

(b) Normalized cell aging.
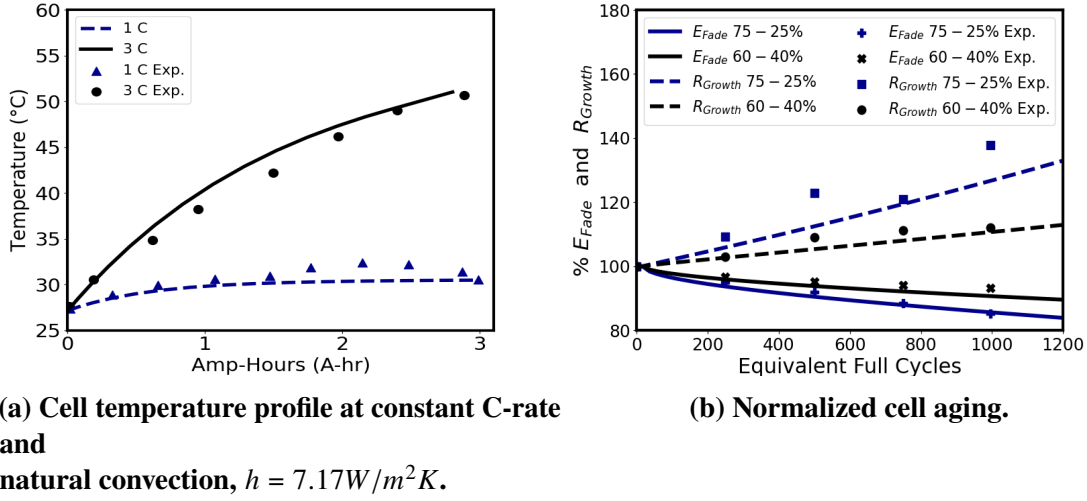
Fig. 9   NMC cell validation.

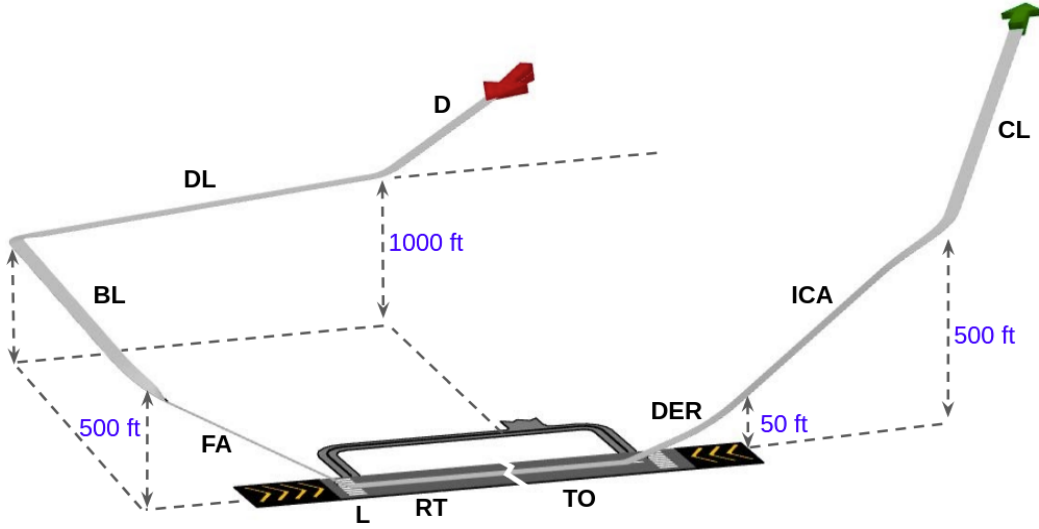5, the specific energy of the battery was 266.25 W-h/kg.

Fig. 10   Typical mission profile of a GA aircraft.

The performance of the aircraft throughout the mission is obtained by running a root-finding algorithm from the Scientific Python (SciPy) [54] package to solve the kinematic equations of motion and the mechanical-electrical relationship that equates the power drawn by the motors to the power supplied by the battery. The heat generated from the battery's internal resistance is coupled with its operating environment and SOC, which in turn is exacerbated at higher charge/discharge rates [55, 56]. Consequently, solving for electrical state variables was done simultaneously with the system of equations representing the force balance of the aircraft. Figure 12 summarizes the temperature and some of the electronic properties of the individual NMC cells and the entire battery
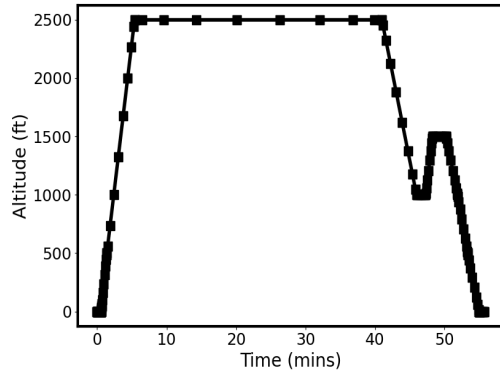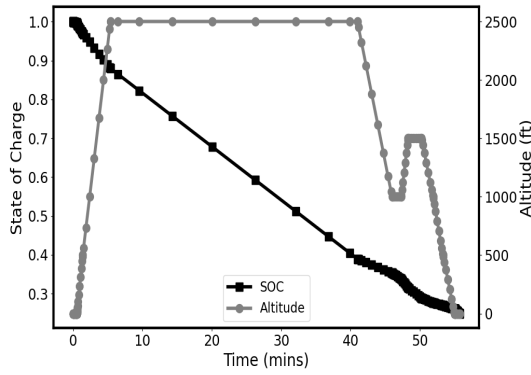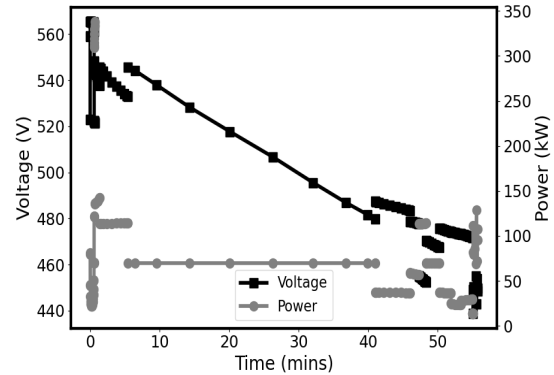
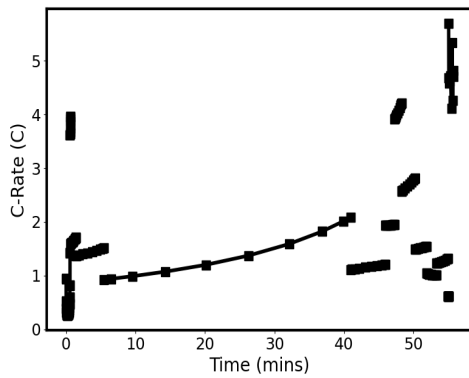**(a)** Aircraft altitude.
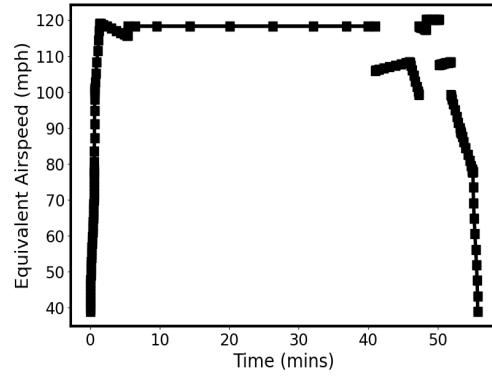
(b) Aircraft airspeed.

Fig. 11   Altitude and airspeed profile of the electric GA aircraft.
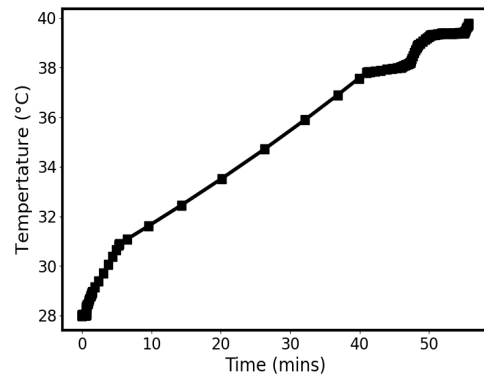

(a) Battery pack SOC.

(b) Battery pack voltage and power draw.

(c) Battery cell C-rate.

(d) Battery cell temperature.

Fig. 12   Battery pack electrical and thermal properties.

Table 7   Electric GA aircraft parameters.

Parameter	Value
General Characteristics	
Passengers	4
Length (m)	8.69
Wingspan (m)	11.4
Reference Area (m^2)	14.75
MTOW (lb)	2186
Battery Capacity (kWh)	130
Powerplant	2 x 3-bladed propellers (1.5m dia.) w/ 60 kW motors
Performance	
Cruise Speed (mph)	155
Range (mi)	130
Service Ceiling (ft)	14,000

pack. As the aircraft climbs through the varying density atmosphere, non-linear throttle profiles arise by virtue of the vehicle meeting the velocities and accelerations specified in the set-up of the mission profile. The discontinuities of V_{UL} in Figure 12b reflect the changes in the power requirements of each flight segment. Additionally, C-rate in Figure 12c refers to the rate at which the cell's energy is being discharged relative to the remaining battery capacity within the cell. Therefore, we expect non-linear profiles even in constant-speed segments such as cruise. A more explicit comparison of these segments is provided in Figure 13. Here, the breakdown of cumulative charge, or charge throughput highlights which segments contribute most to aging as per Equations 15a and 15b. High recorded values of Q predominantly arose in long-duration segments where a nominal amount of current is drawn from the battery such as the final leg of *Climb* and *Cruise*. On the other hand, segments that require large amounts of power such as *Takeoff*, *Departure End of Runway* and *Initial Climb Area* generate the largest amounts of heat within the battery module. This is represented by steep gradients in the respective sections of the curve in Figure 12d.

VII. Battery Sensitivity to Flight Profile and Environmental Conditions

Preliminary results indicate that aircraft performance heavily depends upon the discharge history of the battery. That is, the extent to which a battery ages over its lifetime will change as its internal structure degrades, causing changes in the voltage and current loads required to perform similar maneuvers. Moreover, the full calendar year simulation took approximately 48 hours of wall-clock

Table 8   Flight Segments

Segment	Symbol	Segment Kinematics
Takeoff	TO	Ground-Acceleration
Departure End of Runway	DER	Linear-Speed-Constant-Rate
Initial Climb Area	ICA	Linear-Speed-Constant-Rate
Climb	CL	Constant-Speed-Constant-Rate
Cruise	CR	Constant-Speed-Constant-Altitude
Descent	D	Constant-Speed-Constant-Rate
Baseleg	BL	Linear-Speed-Constant-Rate
Downleg	DL	Constant-Acceleration-Constant-Altitude
Reserve Climb	RCL	Constant-Speed-Constant-Rate
Reserve Cruise	RCR	Constant-Speed-Constant-Altitude
Reserve Descent	RD	Constant-Speed-Constant-Rate
Final Approach	FA	Linear-Speed-Constant-Rate
Landing	L	Ground-Deceleration
Reverse Thrust	RT	Ground-Deceleration

run time on one CPU. It is therefore recommended that any attempt at optimization of the vehicle or battery be first executed through the creation of response surfaces. Subsequent algorithms can be used to determine appropriate values for continuous variables such as the spacing between the individual battery cells within the module and discontinuous variables such as the number of cells in parallel and series.

A prediction of battery energy-capacity fade and internal resistance growth in the NMC cell over a calendar year in San Francisco's climate is provided in Figure 14. The simulated range of each flight per day was 55 miles, which comprised a nominal flight radius of 50 miles from San Francisco International Airport (SFO) and a 10% emergency maneuver. This range encompasses the nearby cities of San Jose, Oakland, Palo Alto and Napa. To account for the time for the battery to recharge at low C-rates, only four flights were simulated per day, each comprising the segments listed in Table 8 along with a final *Ground* segment for charging at 1-C. The impact of recharging on battery life was also captured in the model. Future work will seek to quantify the effect of fast-charging on battery life. The airport departure (TO, ICA, DER) and approach (DL, BL, FA, L, RT) segments were omitted from the range credit. The ambient temperature used in the module's heat transfer model was obtained from the National Centers for Environmental Information [57] and is also shown in this figure. As the aircraft climbs and descends during a flight, the temperature offset due to a change in altitude is also accounted for. From Figure 14a, we see that the continuous operation results in a 25% reduction of battery capacity and an 88% increase in internal resistance.
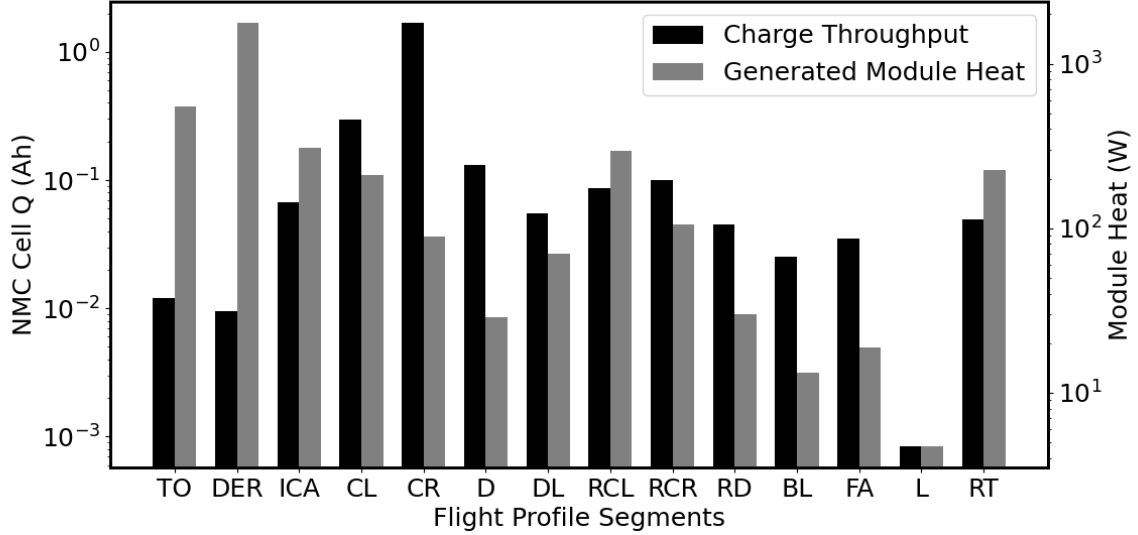
Fig. 13   NMC battery module energy and charge profile per flight segment.

Moreover, Figure 14b portrays the limitations of operation if we were to start with a flight that has an initial range radius of 90 miles representing a mission from San Francisco to Sacramento. We observe that the aircraft can operate flights for 100 days until the lower threshold of 10% SOC is reached at the end of this routine regional flight.

Case 1: Effect of the Rate of Climb & Descent on Battery Life

The impact of the rate of climb on battery life was studied through the analysis of flight profiles with different ascent and descent rates. A total of sixteen combinations were created, see Table 9.

Table 9   Rates of climb & descent studied.

	Rate (ft/min)			
Climb	450	550	650	750
Descent	200	250	320	400

Flight duration, range and cruise altitude were all held fixed for each case, allowing the cruise speed to vary as the only dependent variable. This ensured that the effect of the two parameters under question could be singled out and examined. We gather from Figures 15a and 15b that the mission which minimizes battery degradation is characterized by a high ascent rate in the range of 650-700 ft/min and the lowest descent rate around 200 ft/min. This suggests that a steep climb, followed by a short cruise segment then a gradual descent is the best strategy for prolonging battery life. The benefits of the high ascent rate can be explained as follows. At the beginning of the flight,

21
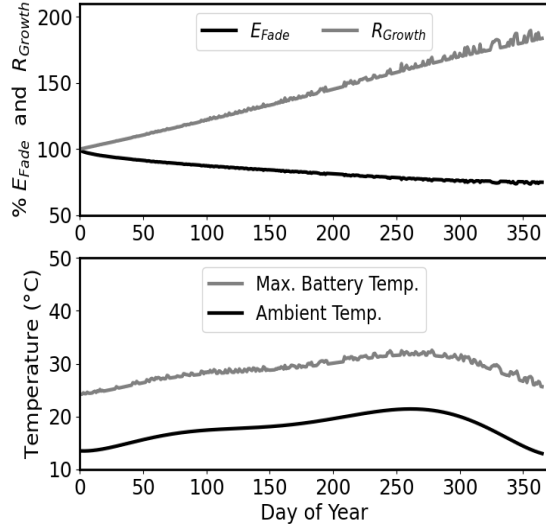
(a) Battery properties.
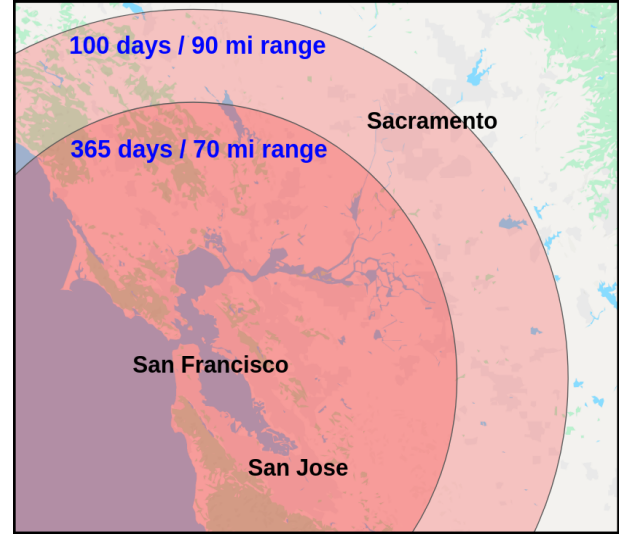
(b) Achievable range of electric GA aircraft.

Fig. 14 Battery pack degradation over one calendar year.

the battery is at 100% SOC, corresponding to the maximum voltage. With higher voltages, lower current loads are required to power avionics and the propulsion system, notably the motors. Near the end of the battery cycle where SOC drops and the maximum voltage of the battery pack decreases, higher current loads are needed to meet propulsion requirements. As pointed out in Section VI, this is reflected in higher C-rates at the end of the mission. Such an effect becomes more pronounced as the battery ages and the voltage associated with a fully changed battery falls below its original value. From the analysis of the cycle aging model in Equation 14c and 14d, we see this is a direct result of quadratic relationship of the difference between the mean voltage and an empirical value (-3.667 in β_{cap} and -3.725 in β_{res}). Effectively, this penalizes long phases at lower voltages. More importantly, we can infer from the small differences in the lost energy-capacity of the most extreme cases that battery life is relatively insensitive to the rate of climb and descent. This, of course, should not come as a surprise given the small allowable margins in the standard maneuvers for this class of aircraft. On the other hand, the vast array of vehicle configurations proposed for UAM will all have eclectic flight profiles that include hover, vertical climb and transition segments which constitute large spikes in the power consumption profile. The differences in both energy-capacity and internal resistance are therefore expected to be more significant.

Case 2: Effect of Range on Battery Life

The effect of range on battery life was then examined. Figure 16a tracks four flight profiles of varying nominal distances. Similar to the previous case outlined above, four identical flights were
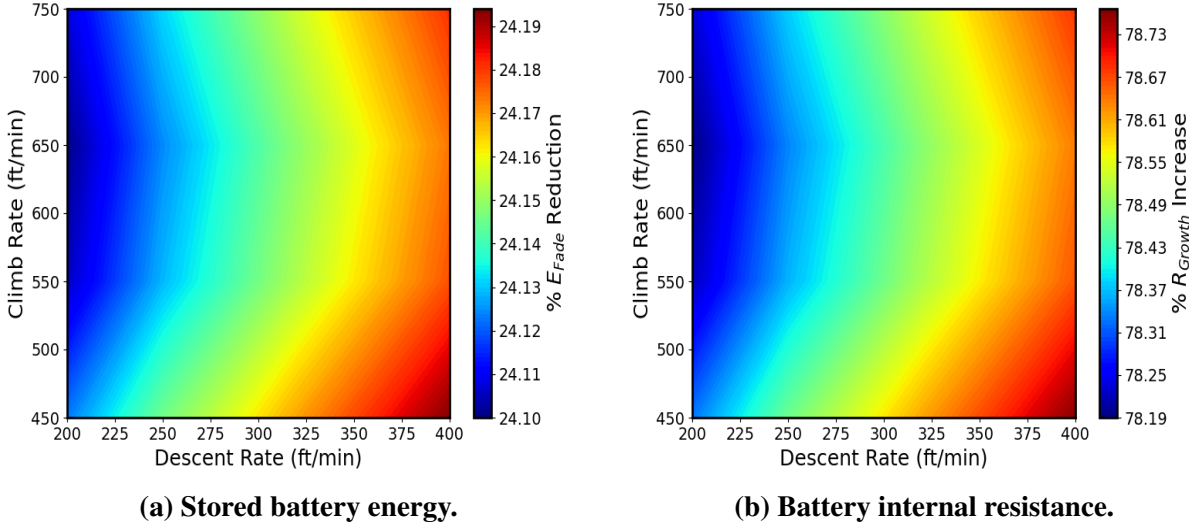
(a) **Stored battery energy.**
(b) **Battery internal resistance.**

Fig. 15   **Effect of climb and descent rate on battery life.**

simulated in each day of the year. We see that there is roughly a 2.5% drop in the energy-capacity every 10 miles. This is accompanied by a 16.5 % increase in internal resistance, implying that this parameter is more susceptible to performance deterioration. Overall, these findings suggest that range has a sizable impact on battery degradation and therefore cannot be omitted during the initial sizing process. When used in conjunction with the energy consumption profile of the aircraft, response surfaces can be created to predict the exact time at which a repeated mission can no longer be executed given the requirements of (1) a reserve flight time that is 10% the nominal range and (2) a lower cut-off bound on the SOC recommended by the battery manufacturer. This lower threshold is typically around 10% and is often placed before the "knee point" in the discharge curve for safe, sustainable operation.

Case 3: Effect of Environmental Conditions on Battery Life

The final study presented in this paper examines the effect of operating temperature on battery life. Here we study how the climates of four major cities, New York (NY), Los Angeles (LA), Houston (HOU) and San Francisco (SF) influence the performance of an electric GA aircraft. As pointed out in the thermal model outlined in Section IV, ambient air is used in the computation of the rate of heat transfer from the tube bundle of lithium-ion cells to the surroundings. The air temperature used as a property of the cooling fluid in the battery module as well as the maximum daily temperature recorded are provided in Figure 17b. The small variations in energy-capacity fade and internal resistance growth tell us that the ambient temperature is not as a significant factor of cell degradation as originally presumed. This further supports the claim by [43] that the thermophysical

23
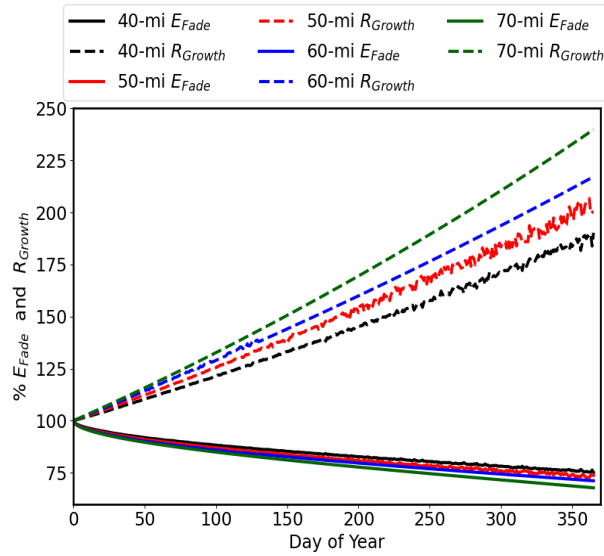
(a) Effect of range on battery SOH.
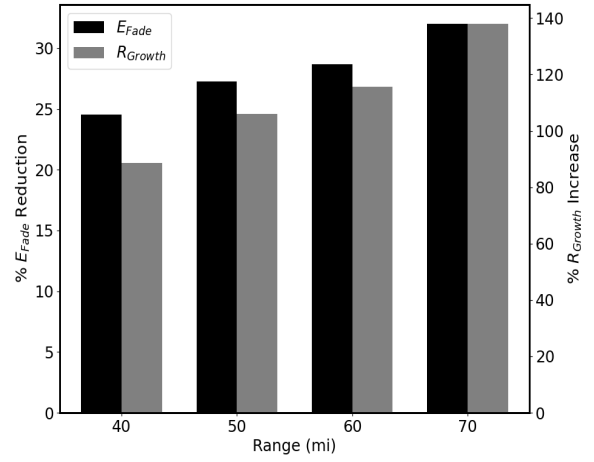
(b) Module and ambient temperature.

Fig. 16   Effect of range on battery life.

properties of the electrolyte and electrodes do not vary significantly between 0°C and 50°C range. Nevertheless, it must be noted that the maximum recorded temperature within the battery is heavily dependent on the module layout and properties of the cooling fluid. A different set of conditions, such as an aligned arrangement of cells, can result in more heat accumulation and consequently accelerated battery degradation.
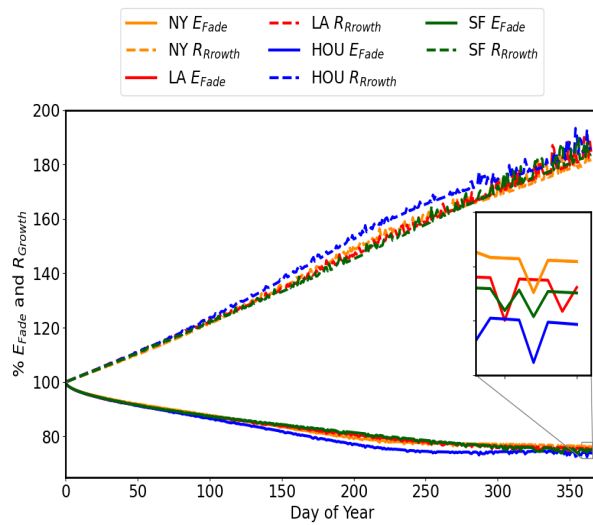
(a) Battery aging parameters.
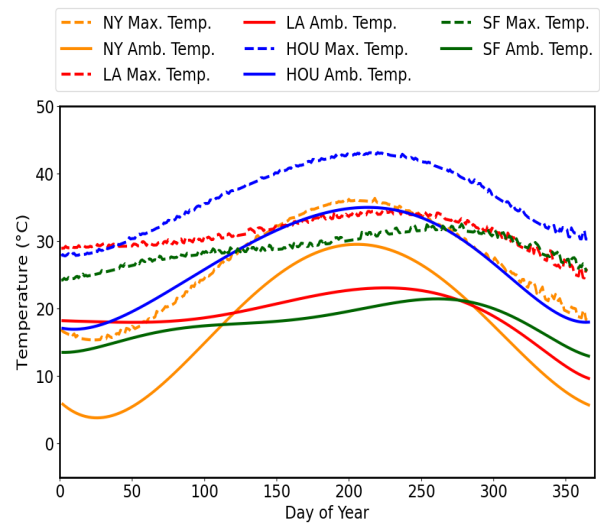
(b) Module and ambient temperature.

Fig. 17   Effect of ambient temperature on battery life.

24

VIII. Concluding Remarks

With lithium-ion batteries proving to be the enabling technology for electric vehicle certification, battery modeling has risen to become a critical component in the design process. The goal of this study was therefore to bridge the gap between the world of conceptual electric aircraft design and the body of existing literature on lithium-ion battery analysis. In this paper, a comprehensive model that encompasses the electrical, thermal and degradation characteristics of the cell and pack for aerospace applications was proposed. Through accurate modeling of a realistic flight profile, it was shown that the battery energy-capacity of an all-electric general aviation aircraft can fall by as much as 25% after one calendar year of operation. These findings suggest that medium-fidelity battery modeling is an essential undertaking for appropriately sizing the battery pack.

One assumption made in this work was the use of a constant specific heat capacity to characterize the thermal load of the NMC cell. In actuality, cylindrical batteries such as the ones used in this work are manufactured by placing multi-layer electrodes and a diaphragm into the electrolyte in the form of a spiral structure. This makes the conductivity inside the battery anisotropic [58]. Additionally, it must be noted that though the model presented in this paper is specific to cylindrical NMC cells, the methodology can be applied to other cell structures (pouch cells) or chemistries (NCA and LFP) once provided with empirical information to update the discharge and aging models. Future work includes relaxing this assumption and implementing a semi-empirical model that has the ability to predict the non-uniform thermal behavior within the cell. This will affect the cell's internal resistance behaviour and holistically the macro-electrical properties of the entire pack. Another area of future work specific to battery modeling is the division of the cells within the module into thermal zones. This can be used in tandem with experimental data to predict heat sinks within the module based on the specific cooling strategy employed. On the aircraft simulation side, there is room for improvement in modeling realistic flight profiles. The inclusion of headwinds, tailwinds and crosswinds, as well as increasing the frequency of flights to mirror a regional taxi service will all significantly impact performance and battery life.

Acknowledgments

References

[1] "Fast Facts on Transportation Greenhouse Gas Emissions," , Jul 2020. URL https://www.epa.gov/greenvehicles/fast-facts-transportation-greenhouse-gas-emissions.

[2] IATA, "2036 Forecast Reveals Air Passengers Will Nearly Double to 7 . 8 Billion," Tech. Rep. 55, IATA, 2017. URL http://www.iata.org/pressroom/pr/Pages/2017-10-24-01.aspx.

[3] Isikveren, A. T., Pornet, C., Vratny, P. C., and Schmidt, M., "Optimization of commercial aircraft using battery-based voltaic-Joule/Brayton propulsion," *Journal of Aircraft*, Vol. 54, No. 1, 2017, pp. 246–261. doi:10.2514/1.C033885.

[4] Hamilton, T., and German, B. J., "Optimal airspeeds for scheduled electric aircraft operations," *Journal of Aircraft*, Vol. 56, No. 2, 2019, pp. 545–555. doi:10.2514/1.C035051.

[5] Traub, L. W., "Optimal battery weight fraction for maximum aircraft range and endurance," *Journal of Aircraft*, Vol. 53, No. 4, 2016, pp. 1176–1178. doi:10.2514/1.C033416.

[6] De Vries, R., Brown, M., and Vos, R., "Preliminary sizing method for hybrid-electric distributed-propulsion aircraft," *Journal of Aircraft*, Vol. 56, No. 6, 2019, pp. 2172–2188. doi:10.2514/1.C035388.

[7] Finger, D. F., Bil, C., and Braun, C., "Initial sizing methodology for hybrid-electric general aviation aircraft," *Journal of Aircraft*, Vol. 57, No. 2, 2020, pp. 245–255. doi:10.2514/1.C035428.

[8] De Vries, R., Hoogreef, M. F., and Vos, R., "Range equation for hybrid-electric aircraft with constant power split," *Journal of Aircraft*, Vol. 57, No. 3, 2020, pp. 552–557. doi:10.2514/1.C035734.

[9] "Why Build an Electric Airplane?" , 2019. URL https://www.nasa.gov/specials/X57/electric-airplane.html.

[10] Clarke, M., Smart, J., Botero, E. M., and Alonso, J. J., "Strategies for Posing a Well-Defined Problem for Urban Air Mobility Vehicles," , No. January, 2019, pp. 1–14. doi:10.2514/6.2019-0818.

[11] Goodenough, J. B., and Kim, Y., "Challenges for Rechargeable Li Batteries," *Chemistry of Materials*, Vol. 22, No. 3, 2010, pp. 587–603. doi:10.1021/cm901452z.

[12] Vetter, J., Novák, P., Wagner, M. R., Veit, C., Möller, K.-C., Besenhard, J., Winter, M., Wohlfahrt-Mehrens, M., Vogler, C., and Hammouche, A., "Ageing mechanisms in lithium-ion batteries," *Journal of power sources*, Vol. 147, No. 1-2, 2005, pp. 269–281.

[13] Wohlfahrt-Mehrens, M., Vogler, C., and Garche, J., "Aging mechanisms of lithium cathode materials," *Journal of power sources*, Vol. 127, No. 1-2, 2004, pp. 58–64.

[14] Cordoba-Arenas, A., Onori, S., Guezennec, Y., and Rizzoni, G., "Capacity and power fade cycle-life model for plug-in hybrid electric vehicle lithium-ion battery cells containing blended spinel and layered-oxide positive electrodes," *Journal of Power Sources*, Vol. 278, 2015, pp. 473–483. doi:10.1016/j.jpowsour.2014.12.047.

[15] Oudalov, A., Buehler, T., and Chartouni, D., "Utility scale applications of energy storage," *2008 IEEE Energy 2030 Conference*, IEEE, 2008, pp. 1–7.

[16] Hannan, M. A., Hoque, M. M., Hussain, A., Yusof, Y., and Ker, P. J., "State-of-the-Art and Energy Management System of Lithium-Ion Batteries in Electric Vehicle Applications: Issues and Recommendations," *IEEE Access*, Vol. 6, 2018, pp. 19362–19378. doi:10.1109/ACCESS.2018.2817655.

[17] Zhang, C., Jiang, J., Zhang, L., Liu, S., Wang, L., and Loh, P. C., "A generalized SOC-OCV model for lithium-ion batteries and the SOC estimation for LNMCO battery," *Energies*, Vol. 9, No. 11, 2016. doi:10.3390/en9110900.

[18] He, H., Xiong, R., and Fan, J., "Evaluation of lithium-ion battery equivalent circuit models for state of charge estimation by an experimental approach," *Energies*, Vol. 4, No. 4, 2011, pp. 582–598. doi:10.3390/en4040582.

[19] Schweighofer, B., Raab, K. M., and Brasseur, G., "Modeling of high power automotive batteries by the use of an automated test system," *IEEE transactions on instrumentation and measurement*, Vol. 52, No. 4, 2003, pp. 1087–1091.

[20] Glass, M. C., "Battery electrochemical nonlinear/dynamic SPICE model," *IECEC 96. Proceedings of the 31st Intersociety Energy Conversion Engineering Conference*, Vol. 1, IEEE, 1996, pp. 292–297.

[21] Feng, F., Lu, R., and Zhu, C., "A combined state of charge estimation method for lithium-ion batteries used in a wide ambient temperature range," *Energies*, Vol. 7, No. 5, 2014, pp. 3004–3032. doi:10.3390/en7053004.

[22] Ng, K. S., Moo, C.-S., Chen, Y.-P., and Hsieh, Y.-C., "Enhanced coulomb counting method for estimating state-of-charge and state-of-health of lithium-ion batteries," *Applied energy*, Vol. 86, No. 9, 2009, pp. 1506–1511.

[23] Zou, Y., Hu, X., Ma, H., and Li, S. E., "Combined State of Charge and State of Health estimation over lithium-ion battery cell cycle lifespan for electric vehicles," *Journal of Power Sources*, Vol. 273, 2015, pp. 793–803. doi:10.1016/j.jpowsour.2014.09.146, URL `http://dx.doi.org/10.1016/j.jpowsour.2014.09.146`.

[24] Di Domenico, D., Fiengo, G., and Stefanopoulou, A., "Lithium-ion battery state of charge estimation with a Kalman filter based on a electrochemical model," *2008 IEEE International Conference on Control Applications*, Ieee, 2008, pp. 702–707.

[25] Plett, G. L., "Extended Kalman filtering for battery management systems of LiPB-based HEV battery packs - Part 1. Background," *Journal of Power Sources*, Vol. 134, No. 2, 2004, pp. 252–261. doi: 10.1016/j.jpowsour.2004.02.031.

[26] Diab, Y., Auger, F., Schaeffer, E., and Wahbeh, M., "Estimating Lithium-Ion Battery State of Charge and Parameters Using a Continuous-Discrete Extended Kalman Filter," *Energies*, Vol. 10, No. 8, 2017. doi:10.3390/en10081075.

[27] Sun, H., and Dixon, R., "Development of cooling strategy for an air cooled lithium-ion battery pack," *Journal of Power Sources*, Vol. 272, 2014, pp. 404–414. doi:10.1016/j.jpowsour.2014.08.107, URL `http://dx.doi.org/10.1016/j.jpowsour.2014.08.107`.

[28] Zhao, J., Rao, Z., Huo, Y., Liu, X., and Li, Y., "Thermal management of cylindrical power battery module for extending the life of new energy electric vehicles," *Applied Thermal Engineering*, Vol. 85, 2015, pp. 33–43. doi:10.1016/j.applthermaleng.2015.04.012, URL `http://dx.doi.org/10.1016/j.applthermaleng.2015.04.012`.

[29] Wang, T., Tseng, K. J., Zhao, J., and Wei, Z., "Thermal investigation of lithium-ion battery module with different cell arrangement structures and forced air-cooling strategies," *Applied Energy*, Vol. 134, 2014, pp. 229–238. doi:10.1016/j.apenergy.2014.08.013, URL `http://dx.doi.org/10.1016/j.apenergy.2014.08.013`.

[30] Alston, E., Jayasinghe, S., Baguley, C., and Madawala, U., "Thermal Management of an Electric Ferry Lithium-Ion Battery System," *2018 IEEE 4th Southern Power Electronics Conference, SPEC 2018*, 2019, pp. 1–4. doi:10.1109/SPEC.2018.8635922.

[31] Spotnitz, R., "Simulation of capacity fade in lithium-ion batteries," *Journal of power sources*, Vol. 113, No. 1, 2003, pp. 72–80.

[32] Ramadass, P., Haran, B., White, R., and Popov, B. N., "Mathematical modeling of the capacity fade of Li-ion cells," *Journal of power sources*, Vol. 123, No. 2, 2003, pp. 230–240.

[33] Xu, B., Oudalov, A., Ulbig, A., Andersson, G., and Kirschen, D. S., "Modeling of lithium-ion battery degradation for cell life assessment," *IEEE Transactions on Smart Grid*, Vol. 9, No. 2, 2018, pp. 1131–1140. doi:10.1109/TSG.2016.2578950.

[34] Todeschini, F., Onori, S., and Rizzoni, G., "An experimentally validated capacity degradation model for Li-ion batteries in PHEVs applications," *IFAC Proceedings Volumes*, Vol. 45, No. 20, 2012, pp. 456–461.

[35] Ecker, M., Nieto, N., Käbitz, S., Schmalstieg, J., Blanke, H., Warnecke, A., and Sauer, D. U., "Calendar and cycle life study of Li(NiMnCo)O2-based 18650 lithium-ion batteries," *Journal of*

Power Sources, Vol. 248, 2014, pp. 839–851. doi:10.1016/j.jpowsour.2013.09.143, URL `http://dx.doi.org/10.1016/j.jpowsour.2013.09.143`.

[36] Schmalstieg, J., Käbitz, S., Ecker, M., and Sauer, D. U., "A holistic aging model for Li(NiMnCo)O2 based 18650 lithium-ion batteries," *Journal of Power Sources*, Vol. 257, 2014, pp. 325–334. doi: 10.1016/j.jpowsour.2014.02.012, URL `http://dx.doi.org/10.1016/j.jpowsour.2014.02.012`.

[37] Automotive & Industrial Systems Company of Panasonic Group, "Technical Information of NCR18650G," `https://www.imrbatteries.com/content/panasonic_ncr18650g.pdf`, . Accessed: 2020-01-30.

[38] Jeon, D. H., and Baek, S. M., "Thermal modeling of cylindrical lithium ion battery during discharge cycle," *Energy Conversion and Management*, Vol. 52, No. 8-9, 2011, pp. 2973–2981. doi:10.1016/j.enconman.2011.04.013, URL `http://dx.doi.org/10.1016/j.enconman.2011.04.013`.

[39] Bernardi, D., Pawlikowski, E., and Newman, J., "General Energy Balance for Battery Systems." *Electrochemical Society Extended Abstracts*, Vol. 84-2, 1984, pp. 164–165.

[40] Mahamud, R., and Park, C., "Reciprocating air flow for Li-ion battery thermal management to improve temperature uniformity," *Journal of Power Sources*, Vol. 196, No. 13, 2011, pp. 5685–5696.

[41] Srinivasan, V., and Wang, C., "Analysis of electrochemical and thermal behavior of Li-ion cells," *Journal of The Electrochemical Society*, Vol. 150, No. 1, 2002, p. A98.

[42] Fan, L., Khodadadi, J., and Pesaran, A., "A parametric study on thermal management of an air-cooled lithium-ion battery module for plug-in hybrid electric vehicles," *Journal of Power Sources*, Vol. 238, 2013, pp. 301–312.

[43] Van Schalkwijk, W., and Scrosati, B., "Advances in lithium ion batteries introduction," *Advances in Lithium-Ion Batteries*, Springer, 2002, pp. 1–5.

[44] Al Hallaj, S., Maleki, H., Hong, J.-S., and Selman, J. R., "Thermal modeling and design considerations of lithium-ion batteries," *Journal of power sources*, Vol. 83, No. 1-2, 1999, pp. 1–8.

[45] Wang, Q., Jiang, B., Li, B., and Yan, Y., "A critical review of thermal management models and solutions of lithium-ion batteries for the development of pure electric vehicles," *Renewable and Sustainable Energy Reviews*, Vol. 64, 2016, pp. 106–128. doi:10.1016/j.rser.2016.05.033.

[46] Williford, R. E., Viswanathan, V. V., and Zhang, J.-G., "Effects of entropy changes in anodes and cathodes on the thermal behavior of lithium ion batteries," *Journal of Power Sources*, Vol. 189, No. 1, 2009, pp. 101–107.

[47] Chin, J. C., Schnulo, S. L., Miller, T. B., Prokopius, K., and Gray, J., "Battery performance modeling on Maxwell X-57," *AIAA Scitech, AIAA 2019-0784*, 2019. doi:10.2514/6.2019-0784.

[48] Bergman, T. L., Incropera, F. P., DeWitt, D. P., and Lavine, A. S., *Fundamentals of heat and mass transfer*, John Wiley & Sons, 2011.

[49] Pastrascu, D., ""Toyota Prius' Battery Recycling Plan," , 2009. URL `https://www.autoevolution.com/news/toyota-prius-battery-recycling-plan-8360.html`, accessed: 2020-05-14.

[50] Zukauskas, A., et al., "Heat transfer from tubes in cross flow," *Advances in heat transfer*, Vol. 8, No. 1, 1972, pp. 93–160.

[51] Trent Lukaczyk and Andrew D. Wendorff and Emilio Botero and Timothy MacDonald and Timothy Momose and Anil Variyar and J. Michael Vegh and Michael Colonno and Thomas D. Economon, and Juan J. Alonso and Tarik H. Orra and Ilario da Silva, Carlos, "SUAVE: An Open-Source Environment for Multi-Fidelity Conceptual Vehicle Design," *AIAA Aviation*, Dallas, TX, 2015.

[52] Vegh, J. M., Silva, C., Johnson, W., Botero, E., Clark, M., Smart, J., and Alonso, J. J., "Current Capabilities and Challenges of NDARC and SUAVE for eVTOL Aircraft Design and Analysis," 2019, pp. 1–15.

[53] Pascale, L., and Nicolosi, F., "Design and aerodynamic analysis of a light twin-engine propeller aircraft," *26th Congress of International Council of the Aeronautical Sciences (ICAS)*, Vol. 1, 2008, pp. 3890–3904.

[54] Virtanen, P., Gommers, R., Oliphant, T. E., Haberland, M., Reddy, T., Cournapeau, D., Burovski, E., Peterson, P., Weckesser, W., Bright, J., van der Walt, S. J., Brett, M., Wilson, J., Jarrod Millman, K., Mayorov, N., Nelson, A. R. J., Jones, E., Kern, R., Larson, E., Carey, C., Polat, İ., Feng, Y., Moore, E. W., Vand erPlas, J., Laxalde, D., Perktold, J., Cimrman, R., Henriksen, I., Quintero, E. A., Harris, C. R., Archibald, A. M., Ribeiro, A. H., Pedregosa, F., van Mulbregt, P., and Contributors, S. . ., "SciPy 1.0: Fundamental Algorithms for Scientific Computing in Python," *Nature Methods*, Vol. 17, 2020, pp. 261–272. doi:https://doi.org/10.1038/s41592-019-0686-2.

[55] Kim, H., Kim, S., Kim, T., Hu, C., and Youn, B. D., "Online thermal state estimation of high power lithium-ion battery," *2015 IEEE Conference on Prognostics and Health Management (PHM)*, IEEE, 2015, pp. 1–6.

[56] Yildiz, M., Karakoc, H., and Dincer, I., "Modeling and validation of temperature changes in a pouch lithium-ion battery at various discharge rates," *International Communications in Heat and Mass Transfer*, Vol. 75, 2016, pp. 311–314.

[57] National Centers for Environmental Information, "Daily Summaries Location Details," , 2019. URL `https://www.ncdc.noaa.gov/cdo-web/datasets/GHCND/locations/CITY:US060031/detail`, accessed: 2019-11-02.

[58] Saw, L., Ye, Y., and Tay, A., "Electrochemical–thermal analysis of 18650 Lithium Iron Phosphate cell," *Energy Conversion and Management*, Vol. 75, 2013, pp. 162–174.